
A New Digital Speckle Correlation Method for Studying the Dynamic Fracture Parameters of Rocks under an Impact Load

Xiaobin Yang^{a,*}, Yanyu Pei^a, Yimin Song^b, and Hongming Cheng^a

^a*China University of Mining & Technology(Beijing), School of Resources and Safety Engineering, Beijing, 100083 China*

^b*North China University of Technology, College of Architecture and Civil Engineering, Beijing, 100041 China*

**e-mail: yangxiaobin02@126.com*

Received December 18, 2018; revised November 18, 2020; accepted March 4, 2021

Abstract—In order to study the dynamic fracture behavior of rocks under an impact load with relatively low impact loading speed, a new method, the Node Interpolation Displacement Representation of Digital Speckle Correlation Method (NIDR-DSCM), was established and a new experimental system was developed. The new DSCM method was used to investigate the dynamic crack displacement field and the experimental system was used to control the impact speed and the startup of the collection system. This new DSCM calculation method was developed and a detailed analysis process was designed to investigate non-uniform deformation and rapid crack propagation in rocks under an impact load. Using images taken with an industrial camera and a high-speed camera and the NIDR-DSCM, the deformation field and the displacement field of dynamic fracture process were obtained, and the crack tip location and displacement width of the crack tip were calculated. The results of the experiments indicate that dynamic fracture propagation in rocks under an impact load can be measured using the new DSCM, which can provide basic parameters for engineering design and construction. The measurement method and experimental impact system of this paper can provide a new approach to investigating the dynamic fracture parameters of rocks under complex physical conditions.

Keywords: digital speckle correlation method, node interpolation displacement representation, dynamic fracture, impact load, crack tip

DOI: 10.3103/S0025654421060224

1. INTRODUCTION

Dynamic fracture propagation in rocks under the effects of an impact load or stress pulses causes issues with operations such as ore and rock crushing, fracturing wells, laying pipe, underground construction, rock blasting, conventional and nuclear explosion protection, and other engineering applications, as well as natural disasters including earthquakes, landslides [1, 2]. Dynamic fracture propagation of rock cracks caused by impact loading is a highly non-linear moving boundary problem, and the existing theoretical analysis only solves a few specific issues concerning the dynamic fracture propagation of rock cracks caused by impact loading. Experimental research not only plays a vital role in the formation and development of dynamic fracture mechanics, but is also the basis for the development and improvement of the dynamic fracture theory of rock cracks caused by impact loading and numerical modeling. Therefore, it is essential to conduct dynamic rock fracture experiments under an impact load to investigate the response and characteristics of the dynamic fracture mechanics.

Dynamic fracture propagation of rock cracks caused by impact loading exhibits two important features, i.e., non-uniform discontinuous deformation in space and the high-speed expansion of cracks with time [3–6] (Xu et al., 2004, Madhu et al., 2007, Sanford 1989, Olden and Patterson 2004). These two characteristics place restrictions on experimental research equipment. First, measurements of the deformation of the entire crack tip field are needed to obtain the non-uniform discontinuous evolution process of the crack tip attachment deformation field dynamic fracture propagation of the rock cracks. In addition, a high-speed data acquisition system is required to record the deformation information and propagation history of the entire crack field during rapid crack propagation. Until now, the existing experimen-

tal methods used to observe dynamic rock fracture propagation have included the electrical measuring method, the acoustic emission method, the thermal infrared method, and the optical measurement method [7–10]. However, in the electrical measuring method and the acoustic emission method, it is difficult to obtain all of the information for the rapid crack propagation field. The thermal infrared method can obtain information for the entire deformation field, but it does not have high-speed data acquisition. Due to the complexity of the experimental conditions required to study dynamic rock fracture mechanics, it is extremely difficult to use interferometry and optical measurement methods such as holographic interferometry, speckle interferometry, and speckle photography to obtain dynamic fracture information for the rock during the experimental process.

Compared with the abovementioned methods for studying dynamic fracture mechanics [11, 12], the Digital Speckle Correlation Method (DSCM) only requires capturing images of the specimen's surface and analyzing them. Then, the deformation field can be determined. Compared with the other optical measurement methods used to make mechanical deformation measurements, the DSCM does not require complicated pre-processing work, and it is possible to directly extract the required deformation information using digital image processing techniques from natural or artificial spots on the surface of an object. Considering the high propagation speed of the crack tip, when a high-speed camera is used, the DSCM can meet the requirements for measuring the dynamic fracture propagation of rock cracks and can capture the and full field dynamic deformation information.

Therefore, in this article, we designed a speed-adjustable drop hammer impact test machine to investigate the dynamic fracture propagation of rock under an impact load with relatively low speed, designed a data acquisition system with a high-speed camera to analyze a high propagation crack, and improved the digital speckle correlation method to calculate the deformation field of rock samples with a dynamic propagation crack. Considering the relative uniformity and processing factors of the rock specimen, the granite was selected and rectangular samples with pre-crack I were manufactured using the designed test machine and measurement method; the dynamic fracture experiments were conducted under impact load. In addition, we quantitatively investigated the evolution of the displacement field of rock crack I caused by impact loading, the crack tip displacement width of the crack's dynamic fracture, the extended history of the crack tip, and the stress intensity factor of the dynamic fracture.

2. NODAL INTERPOLATION DISPLACEMENT REPRESENTATION DSCM

It is problematic for the traditional DSCM [13, 14] to deal with the displacement measurement resolution and the spatial resolution simultaneously. Due to the limited range of the selected window of the traditional DSCM, if the range of the selected window is large, the displacement of the interior point within the window is rougher and the error of the results caused by the displacement model is greater. In order to improve the accuracy of the measurements, it is necessary to change the displacement representation mode of the DSCM, rather than simply reducing the size of the correlation window to improve the spatial resolution. The Mesh-DSCM [15] and the XFEM-DSCM [16, 17] were put forward to solve these problems. Taking into account the advantages of the Mesh-DSCM, in this paper, a new DSCM was developed to measure non-uniform deformation displacement, i.e., the Node Interpolation Displacement Representation DSCM (NIDR-DSCM).

2.1 Node Interpolation Displacement Representation Method for a Non-Uniform Displacement Field

Based on the moving least square method [18, 19], the solution of the displacement field was determined using an approximate function constructed from the nodal displacement. It is assumed that the number of nodes in the measurement area Ω is N and the function to be solved is $u(x)$, the location of the nodes are \mathbf{x}_I ($I = 1, 2, \dots, N$), and the value of $u(x)$ at every node is known, i.e., $u_I = u(\mathbf{x}_I)$. In the measurement area Ω , the function to be solved $u(x)$ can be constructed as a global approximate function $u^h(x)$, so the function to be solved in the closed area Ω_x of the calculated point x can be expressed as

$$u^h(x, \bar{x}) = \sum_{i=1}^m p_i(\bar{x}) a_i(x) = p^T(\bar{x}) a(x), \quad (2.1)$$

in which

$$\begin{cases} p^T = [p_1(\bar{x}), p_2(\bar{x}), \dots, p_m(\bar{x})] \\ a(x) = [a_1(x), a_2(x), \dots, a_m(x)] \end{cases} \quad (2.2)$$

where $\bar{x} = [x, y]^T$ are the spatial coordinates of the nodes in the closed area Ω_x of the calculated point x ; $p_i(\bar{x})$ is the basic function; m is the number of basic functions; and $a_i(x)$ is the coefficient to be solved for. The basic function $p_i(\bar{x})$ must meet the following condition

$$\begin{cases} p_1(\bar{x}) = 1 \\ p_i(\bar{x}) \in C^k(\Omega), \quad i = 1, 2, \dots, m, \end{cases} \quad (2.3)$$

where $C^k(\Omega)$ is the function space with a k order continuous derivative in the area Ω_x . In order to ensure the convergence of the approximate function $u^h(x)$, the basic function must be fully polynomial. Under the two-dimensional condition, the basic function $p_i(\bar{x})$ will be

$$p(\bar{x}) = (1, \bar{x}, \bar{y}), \quad m = 3 \quad (2.4)$$

$$p(\bar{x}) = (1, \bar{x}, \bar{y}, \bar{x}^2, \bar{x}\bar{y}, \bar{y}^2), \quad m = 6 \quad (2.5)$$

$$p(\bar{x}) = (1, \bar{x}, \bar{y}, \bar{x}^2, \bar{x}\bar{y}, \bar{y}^2, \bar{x}^3, \bar{x}^2\bar{y}, \bar{x}\bar{y}^2, \bar{y}^3), \quad m = 10. \quad (2.6)$$

The relationship among the number of basic functions m , the k th order of the fully polynomial function, and the dimension n_d of the problem to be solved is

$$m = \frac{(k+1)(k+2)\cdots(k+n_d)}{n_d}. \quad (2.7)$$

Based on the Moving Least Square method (MLS), the coefficient $a_i(x)$ makes the approximate function $u^h(x)$ the best least square approximation of the function $u(x)$ to be solved in the closed area Ω_x of the calculated point x . Thus, the closed area Ω_x of the calculated point x is defined as the domain of the approximate MLS function at this calculated node, or the domain of the calculated point x .

In discretizing the solution domain with N nodes, at every node location x_I , we define a weight equation $w_I(x) = w(x, x_I)$, where the weight equation $w_I(x)$ is greater than zero only around the closed finite area Ω_I with node x_I , i.e., this function is a compact support function. When applying the DSCM, assuming that there are N nodes in closed area Ω_x of the calculated point x , the error weighted sum of the squares of the displacement approximate function $u^h(x, \bar{x})$ at the point $\bar{x} = x_I$ is

$$J = \sum_{I=1}^N w_I(x) [u^h(x, x_I) - u(x_I)]^2 = \sum_{I=1}^N w_I(x) \left[\sum_{i=1}^m p_i(x_I) a_i(x) - u(x_I) \right]^2. \quad (2.8)$$

The matrix form is

$$J = (Pa - u)^T w(x) (Pa - u), \quad (2.9)$$

in which

$$P = \begin{bmatrix} p_1(x_1) & p_2(x_1) & \cdots & p_m(x_1) \\ p_1(x_2) & p_2(x_2) & \cdots & p_m(x_2) \\ \vdots & \vdots & \ddots & \vdots \\ p_1(x_N) & p_2(x_N) & \cdots & p_m(x_N) \end{bmatrix} \quad (2.10)$$

and

$$w_I(x) = \begin{bmatrix} w_1(x) & 0 & 0 & 0 \\ 0 & w_2(x) & 0 & 0 \\ 0 & 0 & \ddots & 0 \\ 0 & 0 & 0 & w_N(x) \end{bmatrix}. \quad (2.11)$$

If J is the minimum value,

$$\frac{\partial J}{\partial a_i(x)} = 0, \quad (2.12)$$

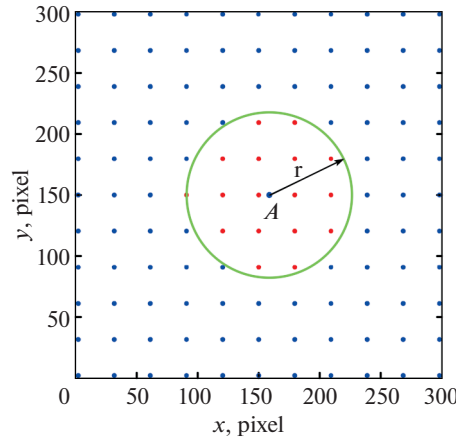


Fig. 1. Schematic diagram of the node influence domain.

and we obtain

$$\sum_{i=1}^m \left[\sum_{I=1}^N w_I(x) p_i(x) p_j(x) a_i(x) \right] = \left[\sum_{I=1}^N w_I(x) p_j(x_I) \right] u_I. \tag{2.13}$$

Equation (13) can be written as

$$A(x)a(x) = B(x)u, \tag{2.14}$$

in which

$$A(x) = \sum_{I=1}^N w_I(x) p(x_I) p^T(x_I), \tag{2.15a}$$

$$B = [w_1(x)p(x_1), w_2(x)p(x_2), \dots, w_N(x)p(x_N)], \tag{2.15b}$$

$$u = [u_1, u_2, \dots, u_N]^T, \tag{2.15c}$$

$$a(x) = [a_1(x), a_2(x), \dots, a_m(x)]. \tag{2.15d}$$

Then, the coefficient to be calculated can be expressed as

$$a(x) = A^{-1}(x)B(x)u. \tag{2.16}$$

Substituting the coefficient function into the unknown displacement function gives

$$u^h(x, \bar{x}) = \varphi(x, \bar{x})u, \tag{2.17}$$

in which the shape function $\varphi(x, \bar{x})$ is

$$\varphi(x, \bar{x}) = p^T(\bar{x})A(x)B(x). \tag{2.18}$$

As described above, the accuracy of the displacement within the solved domain depends on the weight equation and its coefficient. So, the shape function must meet the following conditions [20]:

1. The weight equation must be non-negative in the solved domain.
2. The value of the weight equation at a certain point x is the maximum, while at the other point, if the distance to point x is smaller, the value of the weight equation is much larger; however, if the distance to point x is greater, the value of the weight equation is smaller. When the distance from a certain point to point x is larger than a certain radius, the value of the weight equation is zero, i.e., the weight equation has the compact support property.
3. The weight equation has normalized characteristics.
4. At point x , the coefficient $a(x)$ is unique, i.e., matrix $A(x)$ is reversible.

Generally, the size of the affected area in the node weight equation is determined by the density of nodes, which should have meet following conditions:

1. Every node within the entire solved domain must be covered by at least one influence domain of a certain node.
2. All of the coefficient matrices $A(x)$ used to solve the problem are reversible.
3. In order to maintain the local approximation, the influence region of the node should not be too large.

We use the uniform layout nodes in the solved domain (as shown in Fig.1) with a 300×300 image as an example. First, an 11×11 grid of 121 layout nodes is distributed uniformly over the entire field (the dots in Fig.1) so that the minimum distance between every node is 30 pixels. Assuming a radius R of 70 pixels as the weight equation's influence domain, and using pixel node A as an example point, the coordinate of node A is (160, 150), and all of the nodes that are less than and equal to 70 pixels away from point A are all in the influence domain (the red points in Fig.1). Then, we input the distance d of every node from point A into the weight equation, and the effective weight of every node to point A is calculated.

2.2 NIDR-DSCM Model and the Newton-Raphson Solution

Based on the principle of the DSCM and the information described in 2.1, by establishing a suitable optimization objective and combining it with the node interpolation representation method, an optimization model for the NIDR-DSCM can be established.

Using the least squares correlation coefficient form, the optimization objective of the NIDR-DSCM is

$$C = \frac{\sum_{Sp \in S} \{f(x, y) - g[x + u(x, y, a^I), y + v(x, y, a^I)]\}^2}{\sum_{Sp \in S} f^2(x, y)}, \quad (2.19)$$

where Sp is the coordinate of the pixel; S is the pixel set of the domain to be measured; a^I is the displacement vector of the node; f is the gray of the reference frame; and g is the gray of the target frame.

For a point (x, y) within the reference frame, after deformation, the location of this point within the target frame is (\tilde{x}, \tilde{y}) . The relationship between the reference location and the deformation location of the same point is

$$\begin{cases} \tilde{x} = x + u(x, y, a^I) \\ \tilde{y} = y + v(x, y, a^I) \end{cases}. \quad (2.20)$$

Equation (20) is also the displacement expression. The gray in the reference frame is an integer pixel. However, in the deformed frame, the gray is not always an integer pixel, i.e., after deformation, the point in the reference frame may have no corresponding gray. Therefore, an interpolation processes is required for the points in the deformed frame to obtain the corresponding gray. The following equation for the double three spline interpolation is used

$$g(\tilde{x}, \tilde{y}) = \sum_{i=0}^3 \sum_{j=0}^3 \alpha_{ij} \tilde{x}^i \tilde{y}^j, \quad (2.21)$$

where α_{ij} is the coefficient of the double three spline interpolation.

The NIDR-DSCM requires that every pixel within the domain be measured and a corresponding gray calculation be determined in every time step. The corresponding gray calculation equation is Eq. (19). We can use the node displacement to express the displacement of every integer pixel in the NIDR-DSCM algorithm, using the expression

$$\begin{cases} u(x, y, a^I) = \sum_{i=1}^N \varphi_i(x, y) u_i \\ v(x, y, a^I) = \sum_{i=1}^N \varphi_i(x, y) v_i \end{cases}, \quad (2.22)$$

where N is the number of nodes in the measured domain; $\varphi_i(x, y)$ is the mode shape function; and u_i and v_i represent the displacement components of the i th node.

The matrix expression of all of the nodes in the displacement vector is

$$a^T = [u_1, v_1, u_2, v_2, \dots, u_N, v_N]. \tag{2.23}$$

In Eq. (19), the denominator $1/\sum_{Sp \in S} f^2(x, y)$ is a constant, so

$$C = F \sum_{Sp \in S} \{f(x, y) - g[x + u(x, y, a^I), y + v(x, y, a^I)]\}^2. \tag{2.24}$$

In order to obtain the minimal value of the correlation function C , we must satisfy

$$\nabla C = \left(\frac{\partial C}{\partial a_i} \right)_{i=1,2N} = -2F \sum_{Sp \in S} [f(Sp) - g(Sp, a^I)] \frac{\partial g(Sp, a^I)}{\partial a_j^I} = 0. \tag{2.25}$$

Using the Newton-Raphson iterative method to solve Eq. (25), we obtain the following iterative equation:

$$\nabla \nabla C(a_0)(a - a_0) = -\nabla C(a_0), \tag{2.26}$$

where a_0 is the initial value of node displacement vector a ; and the Hessian matrix $\nabla \nabla C(a_0)$ is

$$\nabla \nabla C = \left(\frac{\partial^2 C}{\partial a_i \partial a_j} \right)_{\substack{i=1,2N \\ j=1,2N}} = \left(\begin{array}{c} -2F \sum_{Sp \in S} [f(Sp) - g(Sp, a^I)] \frac{\partial^2 g(Sp, a^I)}{\partial a_h^I \partial a_k^I} \\ + 2F \sum_{Sp \in S} \frac{\partial g(Sp, a^I)}{\partial a_h^I} \frac{\partial g(Sp, a^I)}{\partial a_k^I} \end{array} \right). \tag{2.27}$$

According to a previous study [21], when a approaches the exact solution and $f(x, y) \approx g(x, y, a^I)$, the Hessian matrix can be expressed as

$$\frac{\partial^2 C}{\partial a_i \partial a_j} = 2F \sum_{Sp \in S} \frac{\partial g(Sp, a^I)}{\partial a_h^I} \frac{\partial g(Sp, a^I)}{\partial a_k^I}, \tag{2.28}$$

in which the gray gradient formula in target frame is

$$\frac{\partial g(Sp, a^I)}{\partial a_k^I} = \frac{\partial g(x, y, a^I)}{\partial \tilde{x}} \frac{\partial \tilde{x}}{\partial a_k^I} + \frac{\partial g(x, y, a^I)}{\partial \tilde{y}} \frac{\partial \tilde{y}}{\partial a_k^I}. \tag{2.29}$$

2.3. Determination of the Shape Function for the Crack Propagation Problem

Section 2.2 gives the general solution of the NIDR-DSCM for investigating crack propagation and determining its characteristics. In this section, we describe the node layout and processing techniques used to deal with the deformation field in the crack propagation problem.

When analyzing crack propagation, the perfect polynomial is used as the basic function. In this paper, the second perfect polynomial is used as the basic function of crack propagation.

$$p(\bar{x}) = (1, \bar{x}, \bar{y}, \bar{x}^2, \bar{x}\bar{y}, \bar{y}^2). \tag{2.30}$$

Many weight equations can satisfy the weight equation selection criteria and the form of these functions is varied. Acceptable weight functions include the exponential, tapered, and spline functions. For crack propagation measurement, we selected the quartic spline function as the weight function, and it has the form

$$w(r) = \begin{cases} 1 - 6r^2 + 8r^3 - 3r^4 & r \leq 1 \\ 0 & r > 1 \end{cases} \tag{2.31}$$

where r is the ratio of the pixel to node distance and the radius of the influence domain.

The crack propagation problem involves a significant discontinuity problem at the interface. Due to this interface problem, both sides of the interface displacement are discontinuous. Taking into account the characteristics on both sides of the interface displacement, while compiling the program and arranging the nodal scheme, the encryption node technique for the area surrounding the interface is implemented, and the node density in the influence domain is held constant. When the influence domain with the node as

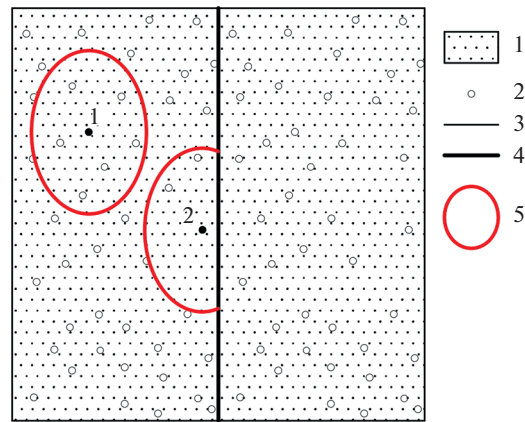


Fig. 2 Treatment of the influence domain in the interface problem:

1—calculation domain; 2—node; 3—boundary of calculation domain; 4—interface; and 5—nodal influence domain.

its center intersects with the interface, the influence domain processing method is used to analyze the interface problem.

As shown in Fig. 2, the two nodes in the calculation domain (node 1 and node 2) are used as an example to illustrate the influence of the interface problem. We regard the line connecting any point with the node as a light ray and the interface as a wall. When the light encounters an interface that it cannot penetrate, it will terminate, i.e., this point is not affected by the node. In the case of discontinuities, the weight equation and the shape function will be set to zero. For example, the lines connecting node 1 and all of the points within its affected domain are not affected by the interface, so all of the points in the node 1 influence domain are related. However, for node 2 in Fig. 2, the points in the influence domain are divided into two categories. The lines connecting node 2 and all of the points on the left side of the interface in the node 2 influence domain are not affected by the interface. These points are related to node 2. The lines connecting node 2 and all of the points on the right side of the interface are affected by the interface. These points have nothing to do with node 2. Thus, the influence domain of node 2 contains only the left side of interface.

In terms of fracture mechanics, the stress field is $1/\sqrt{r}$ singular at the crack tip, while the basis function of the polynomial form has difficulty considering this singularity. Given that in principle, the basis function can use a variety of functions and the moving least squares approximation can provide an accurate reconstruction of the arbitrary items of the basic functions, if we introduce the basic function r into the moving least squares approximation, we will greatly improve the calculation's accuracy. In addition, the displacement and stress distribution are functions of the angle θ at the crack tip. Based on this, we can also introduce a variety of θ functions into the moving least squares approximation. The introduction of these functions is generally referred to as the basic function expansion (or enrichment basis). The expansion of the basic functions can be divided into two categories, the fully extended expansion and the radial expansion. The fully extended expansion is when all functions that comprise the displacement function space are introduced into the basic functions, such as the type I rock crack, and the following basis functions can be used [22, 23]:

$$p^T(x) = \left[1, x, y, \sqrt{r} \cos \frac{\theta}{2}, \sqrt{r} \sin \frac{\theta}{2}, \sqrt{r} \sin \frac{\theta}{2} \sin \theta, \sqrt{r} \cos \frac{\theta}{2} \sin \theta \right]. \quad (2.32)$$

By comparing the extended the moving least squares approximation functions with functions containing only a monomial approximation, it can be seen that the number of unknown node variables does not increase, which is one of the advantages of this method. However, the items of the basic function have increased significantly, there is a large increase in the size of the moving least squares approximation matrix $A(x)$, and a large amount of computing time will be consumed in the verse of matrix A . In addition, as the number of basic function items increases, more nodes are required in the support domain to ensure the non-singularity of matrix A . To deal with the mixed crack types, it is necessary to add other new basic functions. Fortunately, radial expansion can avoid the above problem effectively. Radial expansion considers the crack tip stress field as a continuous function of the angle θ , and it contains a singularity only in

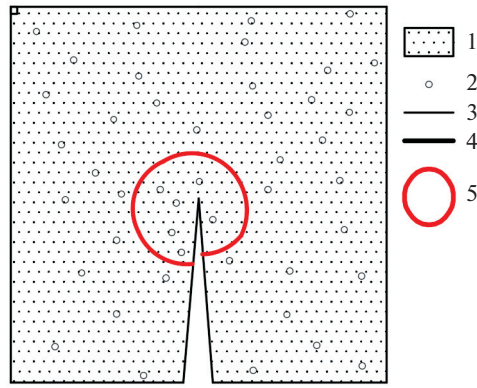


Fig. 3. Treatment of the influence domain during crack propagation:
 1—calculation domain; 2—node; 3—boundary of calculation domain; 4—interface; and 5—nodal influence domain.

the radial direction. Thus, introducing functions that can reflect the singularity in the radial direction solve the problem. The radial extension of the basic function can be written in the following form:

$$p^T(x) = [1, x, y, \sqrt{r}]. \tag{2.33}$$

As shown in Eq. (33), the advantage of radial expansion is that only one r function is added, so the amount of calculation does not increase greatly.

Thus, the node encryption technique is applied to deal with the crack boundary and the area around the crack tip, and an influence domain consistent with the node density is adopted. When the influence domain with the node as its center intersects with the crack, the influence domain processing method is carried out to analyze the crack problems.

As shown in Fig. 3, the weight equation and the shape function are constructed by considering the light diffraction in the corner.

Assuming that the light cannot pass through the discontinuity line, but it can bypass the discontinuity line, the weight equation of the independent variable $d(x)$ can be calculated using

$$d(x) = \left(\frac{d_1(x) + d_2(x)}{d_0(x)} \right)^\gamma d_0(x), \tag{2.34}$$

where $d_0(x) = \|x - x_I\|$, $d_1(x) = \|x_A - x_I\|$, $d_2(x) = \|x - x_A\|$; x_I is the coordinate of node I ; and x_A is the coordinate of node A .

Outside of the influence domain, the weight equation is zero and the shape function should be treated accordingly. When measuring the dynamic rock fracture, cone weight equation form of the weight equation is used:

$$w(r) = \begin{cases} \frac{r_m^2}{r_I^2 + \varepsilon^2 r_m^2} \left(1 - \frac{r_I^2}{r_m^2} \right)^k, & r_I \leq r_m \\ 0 & r_I > r_m \end{cases}, \tag{2.35}$$

where $r_I = \|x - x_i\|$ is the distance between x_i and x ; r_m is the influence radius of node i ; ε is less positive ($\varepsilon = 1.0$); and k is a positive integer ($k = 4$).

2.4 Solution Procedure for the NIDR-DSCM

In this section, the NIDR-DSCM is primarily used for the analysis of non-uniform deformation fields, which entails two issues. First, if the deformation field is homogeneous or uniform, there is no need for NIDR-DSCM processing. Second, the interpolation methods for NIDR-DSCM at different positions are different. Therefore, in solving problems with the NIDR-DSCM, the first step is to determine if the deformation field is uniform or not, and what in the field is not uniform. The next step is to begin the formal NIDR-DSCM calculation according based on the particular different situations. The computational NIDR-DSCM flow chart shown in Fig. 4 illustrates the calculation steps.

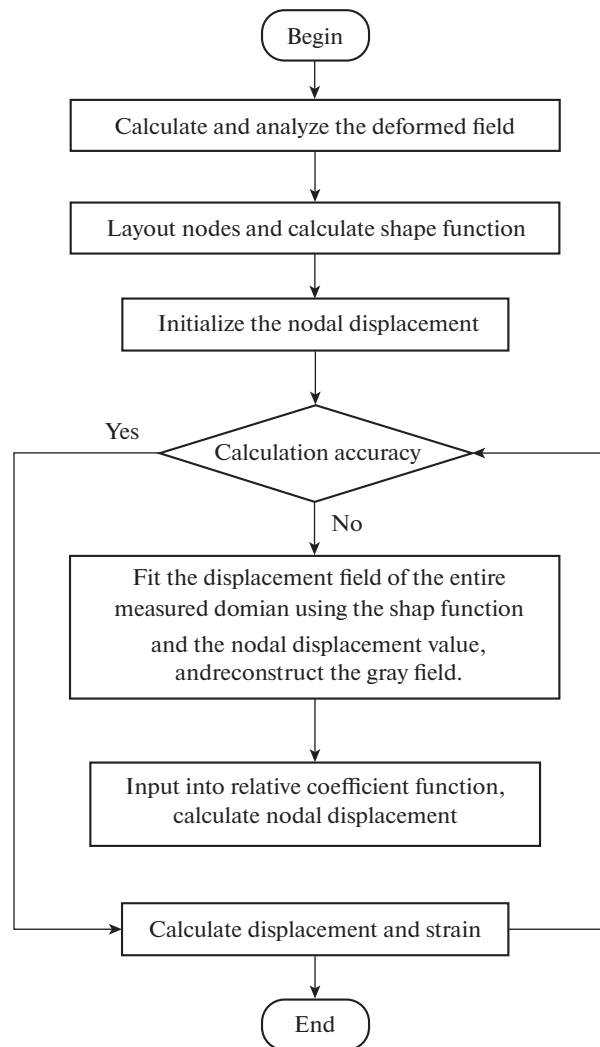


Fig. 4. Computational flow chart of the NIDR-DSCM.

Step one: rough calculation. First, a rough displacement field is obtained using the traditional DSCM process. Using the rough calculation of the displacement field and a speckle image of the experiment, determine whether to use the NIDR-DSCM for analysis. If it is necessary to use the NIDR-DSCM, i.e., the displacement field is discontinuous, determine what kind of layout and interpolation scheme should be selected.

Step two: determine the layout of the nodes. Use the results of step one of the data analysis to determine the nodal distribution. In a uniform deformation area, the nodal distribution is sparse, while in a non-uniform deformation area, the nodal distribution is dense. For a discontinuous deformation area, based on the actual situation, a denser nodal distribution should be used. This step is very important. If the layout is not reasonable, it will offset the advantages of using the NIDR-DSCM to deal with the non-uniform discontinuous field.

Step three: determine the shape function. Based on the results of steps one and two, the corresponding criterion is applied, an appropriate weight equation and node influence domain size are selected, and the shape function matrix of each pixel point is determined.

Step four: node displacement initialization. This step is mainly based on the rough calculation results of step one and makes the calculated displacement of the corresponding nodes in step one smooth through continuous processing to the initial displacement value of each node.

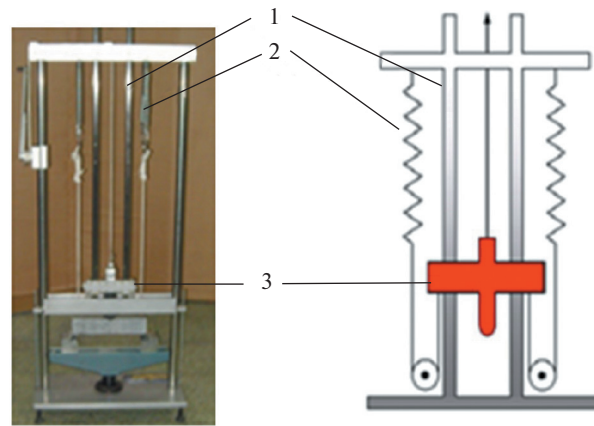


Fig. 5. Test machine and system:

(a) governor drop hammer impact test machine, (b) impact speed regulation system.

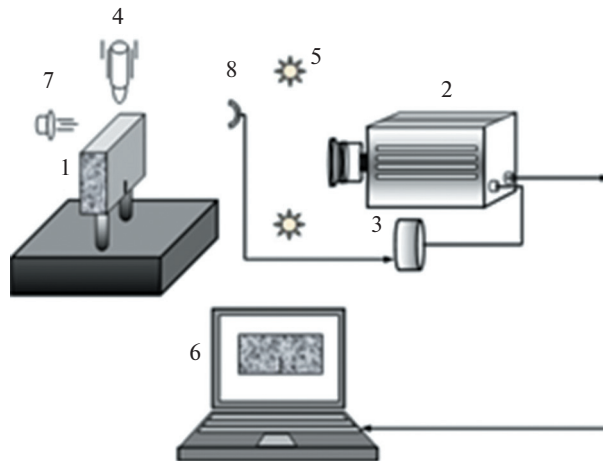


Fig. 6. Schematic diagram of the experimental data acquisition system.

Step five: iterative calculation according using Eq. (26) to meet the conditions until the end of the iteration. The end of the iteration condition is generally set to two times before and after the calculation of the difference between the square and less than 5–10 pixels.

3. EXPERIMENTAL SYSTEM AND EXPERIMENTAL METHODS

3.1 Experimental Loading System

In order to investigate dynamic fracture propagation in rock, taking into consideration the brittle property of rock, according to the principles of the Drop-Weight Tear Test (DWTT) machine, which was used to investigate the metal materials dynamic fracture properties, a newly designed speed-adjustable drop hammer impact test machine was built as shown in Fig. 5a. The loading system of the machine consists of two main parts: the speed-adjustment device and the other is the support system (Fig. 6b). The speed-adjustment device works using springs, and the impact velocity of the drop hammer can be adjusted using different combinations of springs. In this paper, the velocity was adjusted using five groups of springs. At the beginning of the experiment, the drop hammer was raised to the top of the test machine and the springs were stretched. Then, the drop hammer was released, and the spring groups were restored to their initial positions. Under the combined effects of gravity and the restoring energy of the spring groups, the dropped hammer impacted the specimen. Due to the effect of free-fall and the five spring groups, the adjustable range of the test machine's impact speed is 0–10 m/s. The lower support of the load holding

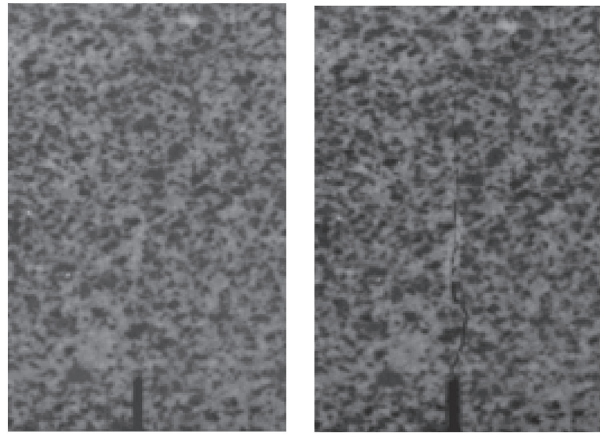


Fig. 7 Dynamic fracture image of the rock specimen:

(a) drop hammer in contact with the rock specimen; (b) cracks extending from rock specimen.

device is a three-point bending support, the drop hammer is the drop hammer device of the standard test machine, and the weight of the drop hammer is 3.2 kg, the distance from the hammerhead to the upper surface of the specimen is 1 m. Loading is provided by the impact of the drop hammer.

The experiments are composed of two main parts: the drop hammer impact speed test and the deformation failure test of rock specimens. In the drop hammer impact speed test, the impact velocity is assessed using the displacement of the white point in the speckle pattern, which is marked at the tip of the drop hammer with lacquer. The deformation failure of the rock specimen can be obtained using the DSCM in conjunction with high-speed cameras photographing the entire impact damage process.

3.2 Experimental Data Acquisition System

The data acquisition system of the dynamic rock fracture experiment has two main requirements. The first is the velocity of the data acquisition. The high-speed cameras must capture speckle images of the entire deformation failure of the dynamic rock fracture process, ensuring adequate view field range and image clarity. This high speed data acquisition provides more detailed information on the dynamic fracture evolution process. The second requirement is the triggering of the high-speed acquisition system, which must be able to accurately record the start time of the dynamic rock fracture. The triggering of the high-speed camera uses a newly designed optoelectronic trigger system, and its triggering mode is pre-trigger. The optoelectronic trigger system includes two inductive components, i.e., a laser head and photo resistance, which are placed on either side of the impact test machine. At the initial time, the photo resistance receives the laser's irradiation and remains closed, and then, the drop hammer begins to fall. When the distance between the hammerhead and the upper surface of the specimen is 10 mm, the drop hammer blocks the laser beam and the photo resistance switches to open, generating a step signal. The signal is sent to the input terminal of the comparator chip, and the comparator generates a standard TTL pulse voltage when the signal reaches the threshold value that the comparator sets, thereby triggering the high-speed camera to start recording the experimental speckle images. The experimental data acquisition system is shown in Fig. 6.

The DSCM analysis is carried out on the speckle images of the dynamic rock fracture experiment collected using the high-speed cameras to obtain the corresponding displacement field. Then, the crack propagation history and the stress intensity factor of the rock fracture are measured.

4. IMPACT FRACTURE EXPERIMENT OF GRANITE SPECIMENS

In this paper, medium-grained granite was selected as the specimen for the dynamic fracture experiment. The granite rock samples were made into 400 mm × 50 mm × 100 mm specimens, and the pre-crack was 10 mm in length and 2 mm in width. The specimen's surface was irradiated using a white light source, the camera and light source were coaxially fixed, and the camera was connected to the image-processing system and the computer display. The camera was adjusted to obtain a clear speckle field within

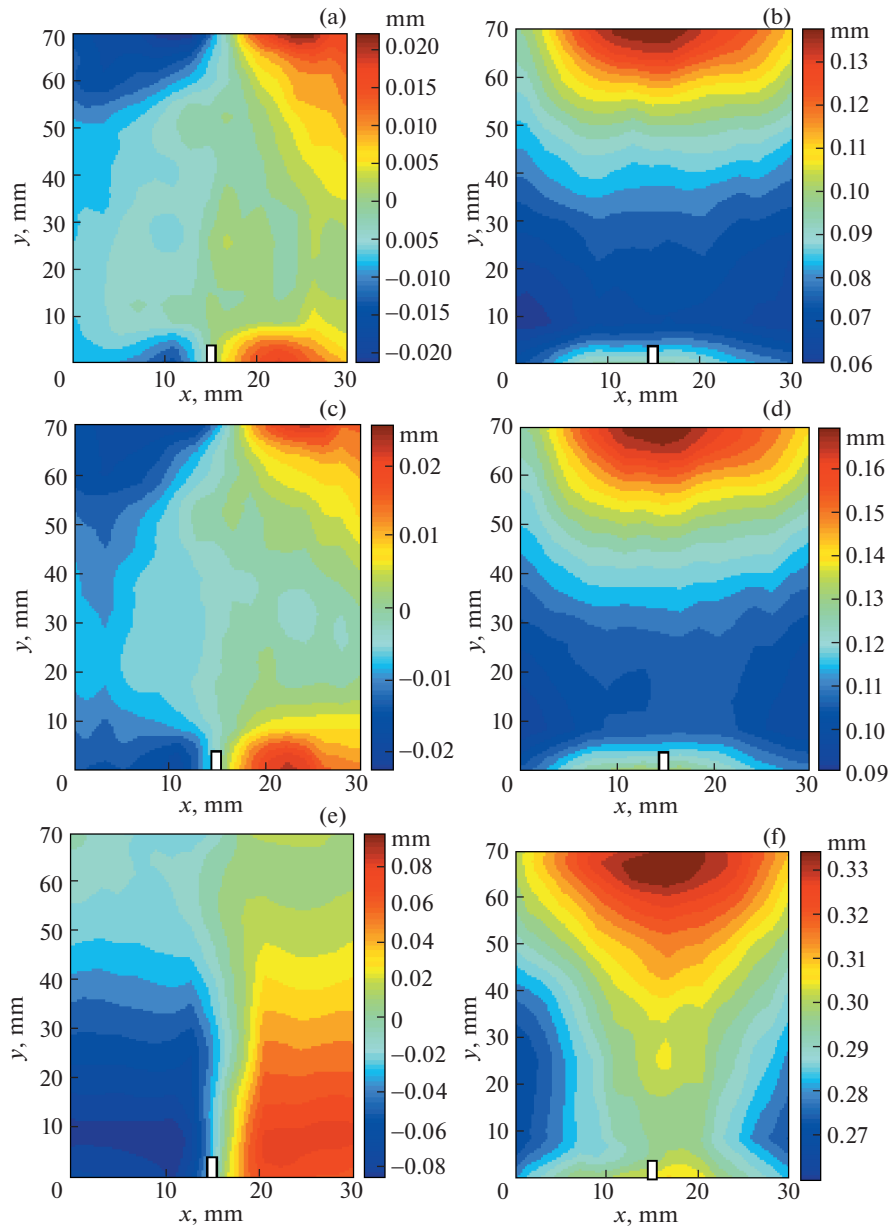


Fig. 8. Evolution of crack propagation-displacement field.

the observing field of view, and the specimen area included in the field of view was $100 \text{ mm} \times 50 \text{ mm}$ with an image resolution of 0.38 mm/pixel . In the experiment, the high-speed cameras recorded the entire process from the pre-crack initiation to the final fracture of the rock specimen with an image acquisition rate of $1 \times 10^5 \text{ frame/s}$. One hundred speckle images were selected and saved, and the corresponding displacement field of the deformation process was obtained by conducting correlation calculations using the collected speckle images.

Figure 7 shows the speckle images of the dynamic fracture process collected by the high-speed camera. Figure 7a is the speckle field when the drop hammer touches the specimen. After the drop hammer touches the upper surface of the rock specimen, by comparing two consecutive speckle images, the gray's significant changes can be found on the contact side, and the position of the gray's change constantly moves down, indicating that the shock wave spread downward from the contact face. Nine microseconds after the drop hammer touched the specimen, cracks appear at the tip of the rock pre-crack and the pre-crack begins to propagate. The impact failure process of fragile rock materials is very fast and it takes $\sim 6 \mu\text{s}$

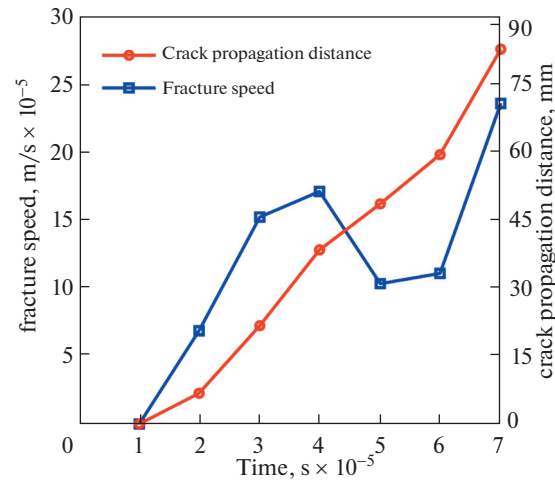


Fig. 9. Rock crack extension history.

to progress from pre-crack initiation to the crack fully penetrating the specimen. Figure 7b shows the speckle image of the cracked rock specimen, clearly showing the expansion of the crack.

The dynamic rock fracture evolution process can be described by the displacement field calculated from the speckle images. Figure 8 shows the dynamic rock fracture displacement field at three moments. Time 1 occurs $8 \mu s$ after the drop hammer touches the upper surface of the specimen when the specimen has undergone an obvious u, v displacement, but no crack propagation has occurred. Time 2 occurs $1 \mu s$ after time 1 when the cracks have extended by 6.8 mm and an increase in the u, v displacement has occurred. Time 3 occurs $5 \mu s$ after the crack begins to extend when the cracks have extended by 60.44 mm and an obvious increase in the u, v displacement has occurred. The displacement of the specimen mainly results from the expansion of the cracks.

5. RESULTS AND DISCUSSION

5.1 Crack Tip Propagation Process

Based on the analysis of the speckle images collected in the dynamic rock fracture experiments, the propagation history of the rock crack tip was studied using the variation law of the crack propagation speed and the crack propagation distance during loading. Figure 9 shows the evolution curves for the crack propagation speed and the crack propagation distance, in which the x-axis represents time, the left vertical axis represents the crack propagation speed (squares), and the right vertical axis represents the crack propagation distance (circles). From Fig. 9, it can be found that the crack propagation distance is approximately linear with the time increasing, especially in the late stage of crack propagation. And to the crack propagation speed, during the initial propagation process, the crack propagation speed is very low, and then, as the crack grows, the crack propagation speed increases, in the last, the maximum crack propagation speed is larger than 2000 m/s at an impact loading speed of 4.5 m/s.

The x-axis represents time, the left vertical axis represents the crack propagation rate (squares), and the right vertical axis represents the crack propagation distance (circles)

Analyzing all the experiments under different impact loading speed, from the pre-crack's crack initiation to the time when the crack fully penetrates the specimen, the crack propagation distance increases approximately linearly with time increasing, the crack propagation speed increases with the impact loading speed increasing, and the average velocity of the crack propagation is greater than 1000 m/s under the effect of impact loading with medium and low velocities.

5.2 Measuring the Displacement Width of the Crack Tip

According to the evolution of the displacement field of the dynamic rock fracture process, the displacement width of the crack tip of the dynamic fracture was studied. Five pairs of pixels were selected on both sides of the crack tip, and the u and v values, i.e., the displacement component of the crack tip, are represented with their average displacement components. The displacement width of the crack tip is defined as

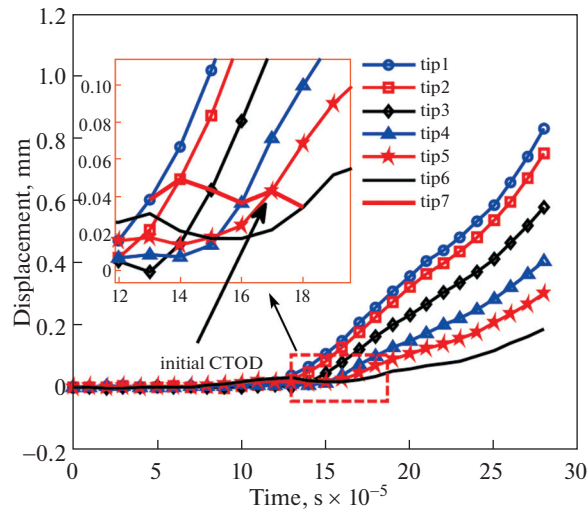


Fig. 10. Displacement width evolution of rock crack tip.

the difference between the u displacement components of both sides of the crack, and then, the data is plotted.

Figure 10 shows the evolution curve of the crack displacement width during loading, in which the x -axis represents the experimental loading time and the y -axis represents the crack displacement width. The curves plots the displacement width of the crack tip at six different times under impact loading. Crack tip 1 is the position of the pre-crack tip, and crack tips 2–6 are the positions of the crack tip from the first propagation to the fifth propagation. In Fig. 10, when the pre-crack extends to crack tip 2, the crack displacement width of crack tip 1 is 0.04 mm. When the crack extends from crack tip 2 to crack tip 3, the crack displacement width of crack tip 2 is 0.046 mm. When the crack extends from crack tip 3 to crack tip 4, the crack displacement width of crack tip 3 is 0.041 mm. When the crack extends from crack tip 4 to crack tip 5, the crack displacement width of crack tip 4 is 0.038 mm. When the crack extends from crack tip 5 to crack tip 6, the crack displacement width of crack tip 5 is 0.039 mm. When the crack extends from crack tip 6 to the boundary of the specimen, the crack displacement width of crack tip 6 is 0.034 mm. According to all of these displacement width values, under the conditions required for the experiment, the crack displacement width of dynamic rock fracture is greater than 0.034 mm; and when the crack displacement width is smaller than this value, crack propagation does not occur.

The x -axis represents the experimental loading time and the y -axis represents the crack displacement width.

6. CONCLUSION

Taking the measuring accuracy and the propagation speed of the rock dynamic fracture problem into consideration, a new Digital Speckle Correlation Method-NIDR-DSCM was developed and a new experimental system was designed. By applying the NIDR-DSCM and experimental system, the I-style-fracture experiment on granite samples under drop hammer impact was conducted to determine the properties of dynamic rock fracture. The following conclusions are drawn:

(1) Using the designed impact loading test equipment and the high-speed camera, the evolution of the displacement field during the crack growth process was determined and the crack propagation history was captured under different impact loading speed.

(2) Applied the new Digital Speckle Correlation Method-NIDR-DSCM, the dynamic rock fracture displacement field and deformation field were analyzed, the dynamic fracture speckle images and the experimental results were calculated, and the crack tip displacement width and the crack propagation location were obtained.

(3) Analyze the experiments results under different impact loading speed, the crack propagation speed can exceed 2000 m/s, and the crack propagation speed increases with the impact loading speed increasing.

Based on our results, the new Digital Speckle Correlation Method-NIDR-DSCM can be used to analyze dynamic rock fracture caused by impact loading, and this method coupled with the designed test system can investigate the crack propagation of rocks under different impact speed, which can provide reference for dynamic crack propagation in geotechnical engineering topics, including rock breaking and hydraulics.

FUNDING

This study was supported by the National Natural Science Foundation of China (grant no. 50904071, 51274207) and the Fundamental Research Funds for the Central Universities (grant no. 2020YJSAQ09).

REFERENCES

1. Z. H. Liu, D. Xie, Y. H. Wang, and L. C. Li, *Engineering Dynamic Fracture Mechanics* (Huazhong Uni. Sci. Techn., Wuhan of China, 1996).
2. M. F. Kanninen and C. H. Popelar, *Advanced Fracture Mechanics* (Oxford Uni. Press, New York, 1985).
3. X. H. Xu, S. P. Ma, M. F. Xia, et al., “Damage evaluation and damage localization of rock,” *Theoret. Appl. Fracture Mech.* **42** (2), 131–138 (2004).
<https://doi.org/10.1016/j.tafmec.2004.08.002>
4. Madhu S. Kirugulige, Hareesh V. Tippur, and T. S. Denney, “Measurement of transient deformations using digital image correlation method and high-speed photography: application to dynamic fracture,” *Appl. Optics.* **46** (22), 5083–5096 (2007).
<https://doi.org/10.1364/AO.46.005083>
5. R. J. Sanford, “Determining fracture parameters with full-field optical methods,” *Exp. Mech.* **29** (3), 241–247 (1989).
6. E. A. Patterson and E. J. Olden, “Optical analysis of crack tip stress fields: a comparative study,” *Fatigue Fract. Eng. Mater. Struct.* **27** (7), 623–636 (2004).
<https://doi.org/10.1111/j.1460-2695.2004.00774.x>
7. K. Ravi-Chandar and W.G. Knauss, “An experimental investigation into dynamic fracture: I. Crack initiation and arrest,” *Int. J. Fracture.* **4**, 247–262 (1984).
<https://doi.org/10.1007/BF00963460>
8. S. Muralidhara, B.K. Raghuprasad, Hamid Eskandari, and B.L. Karihaloo, “Fracture process zone size and true fracture energy of concrete using acoustic emission,” *Constr. Build. Mater.* **24** (4), 479–486 (2010).
<https://doi.org/10.1016/j.conbuildmat.2009.10.014>
9. L. X. Wu, C. Y. Cui, N. G. Geng, and J. H. Wang, “Remote sensing rock mechanics (RSRM) and associated experimental studies,” *Int. J. Rock Mech. Min.* **37** (6), 879–888 (2000).
[https://doi.org/10.1016/S1365-1609\(99\)00066-0](https://doi.org/10.1016/S1365-1609(99)00066-0)
10. J. F. Huang, G. L. Chen, Y. H. Zhao, and R. Wang, “An experimental study of the strain fields development prior to failure of a marble plate under compression,” *Tectonophysics.* **175**, 269–284 (1990).
11. S. P. Ma, X. H. Xu, and Y. H. Zhao, “The Geo-DSCM system and its application to the deformation measurement of rock materials,” *Int. J. Rock Mech. Mining Sci.* **41** (3), 411–412 (2004).
<https://doi.org/10.1016/j.ijrmms.2003.12.007>
12. J. Rethore, A. Gravouil, F. Morestin, and A. Combescure, “Estimation of mixed-mode stress intensity factors using digital image correlation and an interaction integral,” *J. Fract.* **132** (1), 65–79 (2005).
<https://doi.org/10.1007/s10704-004-8141-4>
13. J. Xu, X. F. Xiang, H. Wang, et al., “Experimental study on rock deformation characteristics under cycling loading and unloading conditions,” *Chin. J. Rock Mech. Eng.* **25** (Supp.1), 3040–3045 (2006).
14. I. Yamaguchi, “A laser-speckle strain gauge,” *J. Phys. E: Sci. Instr.* **14**, 1270–1273 (1981).
<https://doi.org/10.1088/0022-3735/14/11/012>
15. Y. F. Sun, J. H. L. Pang, C. K. Wong, and F. Su, “Finite element formulation for a digital image correlation method,” *Appl. Optics* **44** (34), 7357–7363 (2005).
<https://doi.org/10.1364/AO.44.007357>
16. J. Réthoré, F. Hild, and St. Roux, “Shear-band capturing using a multiscale extended digital image correlation technique,” *Comput. Methods Appl. Mech. Eng.* **196**, 5016–5030 (2007).
17. J. Réthoré, St. Roux, and F. Hild, “From pictures to extended finite elements: extended digital image correlation (X-DIC),” *C. R. Mecanique.* **335** (3), 131–137 (2007).
18. P. Lancaster and K. Salkauskas, “Surfaces generated by moving least squares methods,” *Math. Comput.* **37** (155), 141–141 (1981).

19. T. Belytschko, Y. Y. Lu, L. Gu, and M. Tabbara, "Element-free Galerkin methods for static and dynamic fracture," *Int. J. Solids Struct.* **32** (17–18), 2547–2570 (1995).
<https://doi.org/10.1364/AO.44.007357>
20. C. J. Coleman, "On the use of radial basis functions interpolation of scattered data," *IMA J. Num. Anal.* **13**, 13–27 (1993).
21. G. Vendroux and W. G. Knauss, "Submicron deformation field measurements: Part 2. Improved digital image correlation," *Exp. Mech.* **38**, 86–92 (1998).
<https://doi.org/10.1007/BF02321649>
22. N. Moes, J. Dolbow, and T. Belytschko, "A finite element method for crack growth without remeshing," *Int. J. Num. Met. Eng.* **46**: 131–150 (1999).
23. J. Dolbow, N. Moes, and T. Belytschko, "An extended finite element method for modeling crack growth with frictional contact," *Comp. Meth. Appl. Mech. Eng.* **190** (51–52), 6825–6846 (2001).
[https://doi.org/10.1016/S0045-7825\(01\)00260-2](https://doi.org/10.1016/S0045-7825(01)00260-2)